INORGANIC CHEMISTRY FRONTIERS

RESEARCH ARTICLE

View Article Online
View Journal | View Issue

Cite this: *Inorg. Chem. Front.*, 2025, **12**, 7375

Aziridinium cation as a versatile template for hybrid organic–inorganic perovskites of all dimensionalities†

Olesia I. Kucheriv, [a] Oleksandr A. Semenikhin,[a] Yurii S. Bibik,[a] Ivan Bardyk,[b] Sergiu Shova[c] and Il'ya A. Gural'skiy *[a]

Hybrid perovskites form a large group of novel functional materials with diverse structural motifs based on metal-halide polyhedra. Here, we report on a series of hybrid perovskite-like materials of the general formula $(AzrH)_3M_2X_9$ (M = Sb, Bi; X = Cl, Br, and I), the structure of which is templated with the exclusive aziridinium cation $(AzrH)^+$. Notably, single crystal X-ray experiments show that representatives of the reported series exhibit variable crystal structures with different dimensionalities: 0D, 1D, and 2D metal halides. In addition, heterovalent doping of aziridinium lead halides with bismuth allowed us to obtain mixed-metal 3D perovskites as well. $(AzrH)_3M_2I_9$ metal halides form 0D structures in which discrete bi-octahedra are surrounded by aziridinium cations. $(AzrH)_3M_2Br_9$ metal halides form 2D layers separated by $(AzrH)^+$ cations. $(AzrH)_3Bi_2Cl_9$ is isotypical with bromides, while $(AzrH)_3Sb_2Cl_9$ forms 1D polymeric bi-chains. For the obtained set of all dimensionality perovskites, we aimed to establish the correlation among the crystal structure, dimensionality, octahedral connectivity, and halogen type with key optical properties. The optical absorbance of $(AzrH)_3M_2X_9$ metal halides features strong excitonic peaks centered at 330–499 nm with binding energies of 0.06–0.61 eV. The optical band gaps of Sb and Bi aziridinium metal halides were determined to range from 2.61 to 4.09 eV. The lowest obtained band gap for mixed-metal 3D perovskites was found to be 1.49 eV. In addition, doping experiments show a correlation between the dopant dimensionality and the ability to support a 3D framework. DFT calculations were performed in order to study the band structures of $(AzrH)_3Bi_2X_9$ and $(AzrH)_3Sb_2X_9$, and the partial density of states was used to establish which orbitals are located in the vicinity of the Fermi level. This in-depth analysis highlights the transformative potential of $(AzrH)_3M_2X_9$ perovskites for the next-generation optoelectronic devices and their versatility towards both research and practical applications.

Received 7th May 2025,
Accepted 18th July 2025

DOI: 10.1039/d5qi01090j

rsc.li/frontiers-inorganic

Introduction

In materials science and optoelectronics, hybrid organic–inorganic perovskites (HOIPs) have become some of the key materials for research in the 21st century. Their exceptional properties and diverse applications, ranging from photovoltaics and optoelectronics to photocatalysis, have intrigued researchers across different fields.[1] These materials exhibit notable optoelectronic features, including high photoluminescence quantum yields, adjustable band gaps, narrow emission widths, and outstanding charge-carrier mobility.[2] Their tunable luminescence makes halide perovskites promising candidates for light-emitting applications, offering bright and high-color-purity emissions.[3] Recent advancements in fabrication methods, chemical compositions, and phase stabilization techniques have led to highly efficient and cost-effective perovskite-based devices, particularly in solar cells.[4]

Perovskite-like metal halides exhibit different dimensionalities of the inorganic part ranging from zero-dimensional (0D) structures to three-dimensional (3D) frameworks. Such metal halides with crystal structures of different dimensionalities tend to display some characteristic physical properties. For example, 0D metal halides often exhibit high photoluminescence efficiency and are therefore valuable as light sources.[5] These materials are also used for X-ray detection.[6] 1D chained metal halides are often efficient broadband emitters[7] and can also be incorporated into resistive memory devices.[8] 2D layered HOIPs offer exceptional stability and ver-

[a]*Department of Chemistry, Taras Shevchenko National University of Kyiv, Volodymyrska St. 64, Kyiv 01601, Ukraine. E-mail: illia.guralskyi@univ.kiev.ua*
[b]*State Scientific Research Institute of Laboratory Diagnostics and Veterinary and Sanitary Expertise, Donetska St. 30, Kyiv 03151, Ukraine*
[c]*Department of Inorganic Polymers, Petru Poni Institute of Macromolecular Chemistry, Aleea Grigore Ghica Voda 41-A, Iasi 700487, Romania*

† Electronic supplementary information (ESI) available. CCDC 2448195–2448200. For ESI and crystallographic data in CIF or other electronic format see DOI: https://doi.org/10.1039/d5qi01090j

satility.[9] These features in combination with semiconductivity and photoluminescence enhance their performance and longevity in photovoltaics, optoelectronics, and other technological applications.[10] 3D HOIPs are so far the most studied and applied. 3D HOIPs are promising for cost-effective[11] and efficient optoelectronic and photovoltaic devices[12] and stand out thanks to the lowest bandgap values.

The majority of commonly used hybrid perovskites today are lead compounds; however, the high toxicity of this metal stimulates perovskite research towards the development of new representatives of this class that are more environmentally friendly. For example, bismuth-based halide perovskites, known for their Earth-abundant composition,[13] stability and low toxicity,[14,15] offer significant potential in optoelectronics and X-ray detection.[16] In addition, substitutional doping with bismuth enhances the stability of perovskites and device efficiency,[17–19] making them desirable for application in solar cells.[20]

Antimony-based metal halides are typically characterized by low dimensionality,[21] high stability[22] and reduced toxicity[23,24] compared to lead perovskites. These materials present significant potential in optoelectronic applications.[25–27] Antimony-based metal halides stand out due to their strong triplet broadband emission, though effective energy/charge transfer remains a challenge.[28]

Our team has recently shown that the incorporation of aziridinium cations $(AzrH)^+$ supports the formation of 3D semiconducting organic–inorganic materials. $(AzrH)PbX_3$ and $(AzrH)SnX_3$ compounds exhibit low bandgaps and good stability making them promising for further applications in solar cells and light-emitting diodes.[29,30] This paper reports on a series of new aziridinium perovskite-like compounds with bismuth (III) and antimony(III) of the general formula $(AzrH)_3M_2X_9$. Similar to widely used cations methylammonium (MA) and formamidinium (FA), the aziridinium cation (AzrH) supports the formation of perovskite-like structures across a wide range of dimensionalities from 0D to 2D in the $(AzrH)_3M_2X_9$ (M = Sb and Bi) series and 3D in Bi- and Sb-doped $(AzrH)PbX_3$ perovskites. $AzrH^+$ enables the crystallization of diverse architectures with trivalent metals due to its compact size and favorable hydrogen bonding capacity. This allows the same organic cation to template discrete 0D clusters, 1D chains, and 2D layers with different halides and metals. Accessing and controlling this full range of dimensionalities within one chemical platform provides a rare opportunity to reveal how structural confinement and inorganic connectivity govern key properties such as the band gap, exciton binding energy, and photoluminescence behavior. Consequently, the $AzrH^+$ system not only introduces new compositions but also offers a powerful model for studying structure–property relationships across the perovskite dimensionality spectrum. These advancements significantly broaden the spectrum of suitable materials for application in optoelectronic technologies, underscoring the importance and novelty of the aziridinium cation for the construction of versatile hybrid metal halides.

Results and discussion

Single crystal X-ray diffraction

White single crystals of $(AzrH)_3Sb_2Cl_9$ (**SbCl**) suitable for single crystal X-ray diffraction (SXRD) were grown from an acidified solution of $SbCl_3$ and water solution of aziridine using the diffusion crystallization technique as described in details in the ESI.†

SbCl crystallizes in the chiral $P2_12_12_1$ space group of the orthorhombic crystal system (Table 1), which is not very common for achiral cations. Worth noting is that a racemic mixture of enantiomeric crystals is formed according to the refinement. This structure contains two different Sb atoms in the independent unit, both of which have a distorted octahedral environment created by six chlorine atoms (Fig. 1a). These octahedra are corner-shared to form $Sb_2Cl_9^{3-}$ dimeric moieties. Antimony and nine crystallographically independent chlorine atoms are located at general positions. The average Sb–Cl bond lengths are very similar for the two octahedra, being 2.7035 Å for ⟨Sb1–Cl⟩ and 2.7082 Å for ⟨Sb2–Cl⟩. The average angle distortion parameters are $\sigma^2 = \left(\frac{1}{i-1}\right) \times \sum_{i=1}^{i}(\phi_i - 90)^2 = 7.5877$ (where ϕ_i are twelve individual *cis*-X–B–X angles) and 5.0641 for Sb1 and Sb2, respectively. The length distortion parameters are $\Delta = (1/i)\sum_{i=1}^{i}\left(\frac{d_i - d}{d}\right)^2 = 9.450 \times 10^{-3}$ (where d_i are B–X bond lengths and d is the mean B–X bond length) and 10.344×10^{-3} for Sb1 and Sb2, respectively (Table 2).

These anionic $Sb_2Cl_9^{3-}$ moieties are further connected to form 1D zigzag double-chains of corner-shared octahedra which propagate along the *a*-axis (Fig. 1b and c). Three crystallographically independent aziridinium cations are located among the chains and create hydrogen bonds with them. (AzrH)1 creates hydrogen bonds with chlorine atoms from a single chain and is located in inner rectangular voids of 1D double-chains, forming almost equivalent hydrogen bonds with D–H···A angles of 164.2(4)° and 167.9(4)° and D···A distances of 3.170(6) Å and 3.177(7) Å, respectively. Meanwhile, (AzrH)2 is located between chains and is bound to chlorine atoms from two neighboring chains forming two hydrogen bonds with D–H···A angles of 174.1(4)° and 148.8(4)° and D···A distances of 3.308(6) Å and 3.196(6) Å, respectively. (AzrH)3 is also bound to different chains forming two hydrogen bonds with D–H···A angles of 156.2(4)° and 137.1(4)° and with D···A distances of 3.250(7) Å and 3.443(7) Å, respectively. The hydrogen bond geometry is summarized in Table S1.†

Unlike **SbCl**, $(AzrH)_3Bi_2Cl_9$ (**BiCl**) crystallizes in the $P\bar{3}m1$ space group of a trigonal crystal system. In addition, **BiCl** is isostructural to $(AzrH)_3Sb_2Br_9$ (**SbBr**) and $(AzrH)_3Bi_2Br_9$ (**BiBr**) and to $A_3M_2Br_9$ (A = Cs, MA, and FA; M = Sb and/or Bi).[31–33] The description of **BiBr** will be given as an example of these three isostructural compounds.

Table 1 Crystal data and structure refinement parameters for the studied **BiX** and **SbX** perovskites

	BiCl	**BiBr**	**BiI**	**SbCl**	**SbBr**	**SbI**
Empirical formula	$Bi_2C_6Cl_9N_3$	$Bi_2Br_9C_6N_3$	$Bi_2C_6I_9N_3$	$C_6H_{18}Cl_9N_3Sb_2$	$Br_9C_6N_3Sb_2$	$C_6I_9N_3Sb_2$
Formula weight	851.10	1251.24	1674.15	694.78	1076.78	1499.69
Crystal system	Trigonal	Trigonal	Hexagonal	Orthorhombic	Trigonal	Hexagonal
Space group	$P\bar{3}m1$	$P\bar{3}m1$	$P6_3/mmc$	$P2_12_12_1$	$P\bar{3}m1$	$P6_3/mmc$
a (Å)	8.1302(5)	8.3790(8)	8.7295(3)	8.1531(2)	8.4363(16)	8.5753(5)
b (Å)	8.1302(5)	8.3790(8)	8.7295(3)	13.5976(5)	8.4363(16)	8.5753(5)
c (Å)	9.7629(7)	10.2124(7)	22.0367(14)	19.5393(6)	10.1667(15)	21.7548(13)
$\alpha = \beta$ (°)	90	90	90	90	90	90
γ (°)	120	120	120	90	120	120
Volume (Å^3)	558.86(8)	620.93(13)	1454.31(14)	2166.18(12)	626.6(3)	1385.43(18)
Z	1	1	2	4	1	2
$\rho_{calc.}$ (g cm^{-3})	2.529	3.346	3.823	2.130	2.853	3.595
μ (1 mm^{-1})	16.789	28.623	21.632	3.597	16.496	11.973
Crystal size per mm^3	0.15 × 0.06 × 0.06	0.15 × 0.08 × 0.08	0.29 × 0.20 × 0.01	0.15 × 0.05 × 0.02	0.2 × 0.1 × 0.1	0.21 × 0.09 × 0.05
2Θ range for data collection (°)	5.786 to 59.86	3.988 to 57.914	3.696 to 57.878	5.134 to 60.644	4.006 to 57.976	5.486 to 60.55
Reflections collected	2271	1738	4561	16791	1963	6008
Independent reflections (R_{int}, R_{sigma})	584 (0.0288, 0.0281)	589 (0.0441, 0.0617)	722 (0.0537, 0.0473)	5459 (0.0300,0.0385)	596 (0.0823, 0.0982)	764 (0.0333, 0.0199)
Data/restraints/parameters	584/3/20	589/11/28	722/5/24	5459/0/182	596/9/20	764/13/35
Goodness-of-fit on F^2	1.066	1.127	1.114	1.021	1.084	1.145
R_1 [a], wR_2 [b] [$I \geq 2\sigma(I)$]	0.0271, 0.0621	0.0535, 0.1135	0.0460, 0.0897	0.0300, 0.0596	0.0709, 0.1368	0.0368, 0.0835
R_1 [a], wR_2 [b] [all data]	0.0344, 0.0637	0.0769, 0.1225	0.0753, 0.1023	0.0435, 0.0643	0.1591, 0.1719	0.0458, 0.0873
Largest diff. peak/hole (e Å^{-3})	1.50/−0.84	1.68/−1.45	0.87/−1.31	1.19/−0.89	1.90/−1.07	1.43/−0.93

[a] $R_1 = \sum||F_o| - |F_c||/\sum|F_o|$. [b] $wR_2 = [\sum w(F_o^2 - F_c^2)^2/\sum w(F_o^2)^2]^{1/2}$ for $F_o^2 > 2\sigma(F_o^2)$.

Yellow single crystals of $(AzrH)_3Bi_2Br_9$ suitable for single crystal X-ray diffraction were obtained similarly to **SbCl**. The unit cell of **BiBr** contains one crystallographically independent bismuth and two independent bromine atoms (Fig. 2a). In the crystal packing, Bi is surrounded by six bromine atoms in a slightly distorted manner. Three symmetry generated Br1 atoms located in the *fac*-manner are terminal, while symmetry generated Br2 atoms are bridging and connect with neighboring octahedra in corner-sharing mode creating infinite 2D layers with vacancies (Fig. 2b and c). These inorganic layers are parallelly stacked along the c axis mimicking the ABX_3 3D structure but missing every third layer of B-site cations.

The bond length between bismuth and the terminal bromine atoms is 2.707(2) Å, which is notably shorter than the bond length with the bridging atoms −3.0512(6) Å. This discrepancy results in a significant average bond length deviation parameter $\Delta = 3.568 \times 10^{-3}$.

The bond angles in the structure exhibit slight deviations from the ideal values. Specifically, the Br1–Bi–Br1^i angle is 92.80(6)°. Br1–Bi–Br2 and Br2–Bi–Br2^i angles are equal to 90.16(3)° and 86.71(2)°, respectively. The slight distortion of the octahedra is reflected in the relatively small angle distortion parameter σ^2 which is 5.0966.

In the **BiBr** structure, there are two crystallographically independent aziridinium cations, both of which are highly disordered and the selected model is only one of the multiple ways to represent this disorder. Even though hydrogen atoms cannot be localized in these highly disordered cations, N⋯Br distances in a 3.06–3.81 Å range interval indicate the presence of hydrogen bonds in this structure.

Red single crystals of $(AzrH)_3M_2I_9$ (**MI**, M = Sb and Bi) suitable for single crystal X-ray diffraction were grown from HI solutions of MI_3 and water solution of aziridine using the diffusion crystallization technique. Crystal structures of the mentioned compounds are isostructural and were solved in the $P6_3/mmc$ space group. The structures correspond to the $Cs_3Cr_2CI_9$ structural type and are isostructural with $Cs_3Sb_2I_9$ and $Cs_3Bi_2I_9$.[34]

In **BiI**, the crystallographically independent part contains one Bi and two iodine atoms and two aziridinium cations (Fig. 3). In the crystal packing Bi has a distorted octahedral environment created by six iodine atoms. Three symmetry generated I1 atoms located in *fac*-manner are terminal, while symmetry generated I2 atoms ensure face-sharing connection to form $[Bi_2I_9]^{3-}$ dimeric moieties. The structure of **SbI** features similar moieties, however, all the iodine atoms in $[Sb_2I_9]^{3-}$ are disordered between two positions. The octahedral environment in both **BiI** and **SbI** structures is distorted. The distortion in the $[MI_6]^{3-}$ octahedra is most likely due to repulsion between the M^{3+} ions within the $M_2I_9^{3-}$ cluster, which has an M⋯M distance of 4.1195(18) Å and 4.208(2) Å for Sb^{3+} and Bi^{3+}, respectively. This repulsive interaction causes deviations from the ideal octahedral geometry: contraction of the I2–M–I2^i angles for bridging iodine atoms down to 82.88(2)° for **SbI** and 82.72(3)° for **BiI** and an expansion of the I1–M–I1^i angles for terminal atoms up to 100.38(4)° for **SbI** and 93.9(5)° for **BiI**.

Despite the disordered positions of iodine in **SbI**, the M–I–M angles are practically equal in two structures: 80.33(3)° and 80.53(4)° for **SbI** and **BiI**, respectively. As anticipated, the bridging Sb1–I2 bonds (3.1935(15) Å) are longer than the terminal Sb1–I1 (2.8878(9) Å) and the Bi1–I2 bridges (3.2554(12) Å) are slightly longer than the terminal Bi1–I1 bonds (2.9535(13) Å). The averaged angle distortion parameter σ^2 is 42.0212° for **SbI**

Table 2 General information about crystal polyhedra

	BiCl	BiBr	BiI	SbCl		SbBr	SbI
	$P\bar{3}m1$	$P\bar{3}m1$	$P6_3/mmc$	$P2_12_12_1$		$P\bar{3}m1$	$P6_3/mmc$
Space group				Sb1	Sb2		
B–X (Å)	2.548(2)–2.8979(2)	2.7075(19)–3.0512(6)	2.9534(12)–3.2554(12)	2.4170(16) –2.9445(16)	2.4104(18)–3.0678(16)	2.622(2)–3.0582(11)	2.8878(8)–3.1935(9)
cis X–B–X (°)	89.077(9)–91.11(9)	86.713(19)–92.80(7)	82.72(3)–93.91(4)	84.55(5)–92.89(6)	85.68(5)–93.75(7)	87.21(4)–92.08(8)	76.48(4)–99.09(3)
trans X–B–X (°)	178.56(7)	175.70(5)	172.18(4)	174.66(5)–177.44(5)	174.54(6)–178.65(6)	176.56(7)	167.82(3)–172.90(3)
B–X–B (°)	180.0	180.0	80.53(4)	161.65(7); 175.94(6)	180.0	80.33(3)	
⟨B–X⟩ (Å)	2.723	2.8792	3.1044	2.7035	2.7082	2.840	3.0407
$\Delta \times 10^3$ [a]	4.154	3.568	2.364	9.450	10.344	3.3553	2.529
σ^2 [b]	0.0594	5.0966	19.7067	7.5877	5.0641	5.902	42.0212
Volume of polyhedron (Å^3)	26.910(15)	31.760(14)	39.550(12)	26.26(1)	26.42(1)	30.500(15)	36.612(13)–37.187(13)

[a] $\Delta = (1/i)\sum_{i=1}^{i}\left(\frac{d_i - d}{d}\right)^2$ (where d_i are B–X bond lengths and d is the mean B–X bond length). [b] $\sigma^2 = \left(\frac{1}{i-1}\right)\sum_{i=1}^{i}(\phi_i - 90)^2$ where ϕ_i are individual *cis*-X–B–X angles.

Fig. 1 Crystal structure of $(AzrH)_3Sb_2Cl_9$: (a) the coordination environment of Sb. Thermal ellipsoids are represented at the 50% probability level; (b) view along the *a* axis showing the propagation of the double chains; and (c) view of the zigzag-like arrangement of 1D double-chains.

Fig. 2 Crystal structure of $(AzrH)_3Bi_2Br_9$: (a) the coordination environment of Bi. Aziridinium disorder is omitted for clarity. Thermal ellipsoids are represented at the 50% probability level. (b) View along the *ab* plane showing the propagation of 2D layers. (c) View along the *c* axis showing the mutual arrangement of coordination octahedra inside a layer.

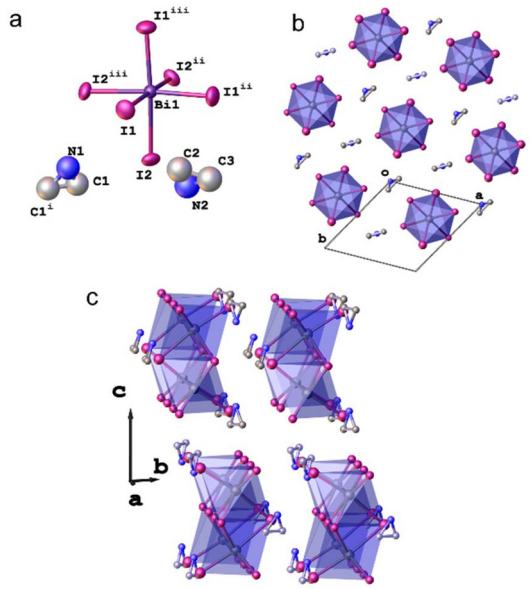

Fig. 3 Crystal structure of $(AzrH)_3Bi_2I_9$: (a) the coordination environment of Bi. Aziridinium disorder is omitted for clarity. Thermal ellipsoids are represented at the 50% probability level. (b) View along the *b* axis showing the mutual arrangement of bi-octahedra. (c) View along the *ab* plane.

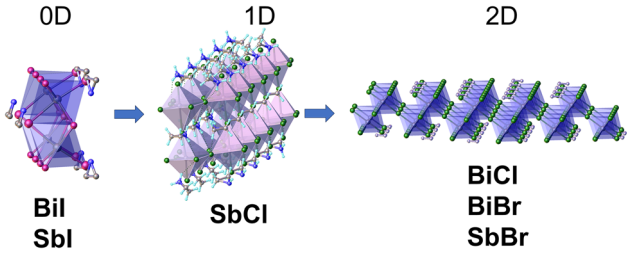

Fig. 4 Comparison of 0D, 1D and 2D frameworks of the reported materials.

compared to σ^2 = 19.7067° for **BiI**, indicating a more significant distortion of the coordination octahedron in **SbI**. Additionally, the average parameter of deviations of bond lengths Δ is slightly larger for **SbI** than for **BiI** and equals 2.529×10^{-3}, 2.364×10^{-3}, respectively.

The negative charge in the structure is balanced by three $(AzrH)^+$ ions, which exhibit significant disorder. Similar to the situation observed in **MBr**, N···I distances indicate the presence of hydrogen bonds in these structures (Table S2†).

Interestingly, popular A-site cations (A = MA, FA, Cs, and AzrH) form isostructural 3D perovskites with lead and tin iodides (which crystalize in the $Pm\bar{3}m$ space group);[29,30,35–38] however, in combination with Sb and Bi the formation of compounds which crystalize in different space groups has been reported: $P6_3/mmc$ for $MA_3Bi_2I_9$[39] and $Cs_3M_2I_9$,[34] and $P6_3mc$ for $FA_3Bi_2I_9$.[40]

Meanwhile, larger A-site cations like guanidinium (GA),[41] trimethylsulfonium,[42] and imidazolium[43] cannot stabilize the "classical" 3D perovskite structure with tin and lead iodides, however, with Sb and Bi the abovementioned cations form compounds which are isostructural with $(AzrH)_3M_2I_9$.

A comparative schematic showing the difference between 0D, 1D and 2D frameworks in materials reported in this work is given in Fig. 4.

Optical properties

The optical characteristics of $(AzrH)_3Bi_2X_9$ and $(AzrH)_3Sb_2X_9$ (X = Cl, Br, and I) perovskites were examined using UV–vis spectroscopy. Powder samples of the reported perovskites were used for optical measurements. Correspondence between the powder samples and the studied single crystals was confirmed by PXRD measurements (Fig. 5).

UV-vis spectra of the $(AzrH)_3M_2X_9$ series are characterized by the presence of absorption peaks, which are indicative of strong electron–hole coupling resulting in the formation of self-trapped excitons,[44,45] and continuous bands which characterize optical band gaps of these materials (Fig. 6 and Fig. S1†). In such materials, where bound excitons can be observed, the difference between exciton energy (E_{ex}) and band gap (E_g) characterizes exciton binding energy $E_B = E_g - E_{ex}$.[46] Sometimes for materials where bound excitons are present, the band gap is mistakenly set to the onset of the excitonic band and this leads to significant underestimation of this value.

Distinct absorption peaks can be found for $(AzrH)_3Bi_2X_9$ at 359 nm and 499 nm for Cl and I, respectively. Simultaneously, $(AzrH)_3Sb_2X_9$ displays absorption peaks at 330 nm and 445 nm for Cl, and I, respectively. Notably, both $(AzrH)_3M_2Br_9$ perovskites feature two absorption peaks at 425 and 389 nm for $(AzrH)_3Bi_2Br_9$ and at 424 and 388 nm for $(AzrH)_3Sb_2Br_9$. Such an effect has been previously observed for layered 2D perovskites. It was established that the shorter wavelength excitonic peak originates from isolated 2D layers, while the lower energy peak is associated with the edge states.[47]

The shift of absorption maxima upon substitution of halogen results in a distinct colour change from white for Cl-based samples to yellow and red for Br and I-based perovskites, respectively (Fig. 6(c)).

The E_{ex}, E_g and E_B values of the reported materials were obtained from Tauc plots (Fig. 6(d–i)) and are summarized in Table 3. The Tauc exponent for direct allowed transitions was used for calculations. The direct bandgap semiconducting nature of the reported perovskites was confirmed by DFT calculations, as shown further in the text.

There are many factors that influence the band gap.[48] The main ones include the connectivity of the inorganic lattice, which controls the band structure, leading to an increase in the energy gap with the decrease of dimensionality.[49] Additionally, the energy of the halogen's p orbital significantly contributes to the formation of the conduction band (CB). Upon transition from **BiCl** to **BiBr**, which are isostructural, the red shift of the band gap originates from the difference in the energy level of 3p and 4p orbitals of the halogen. In contrast,

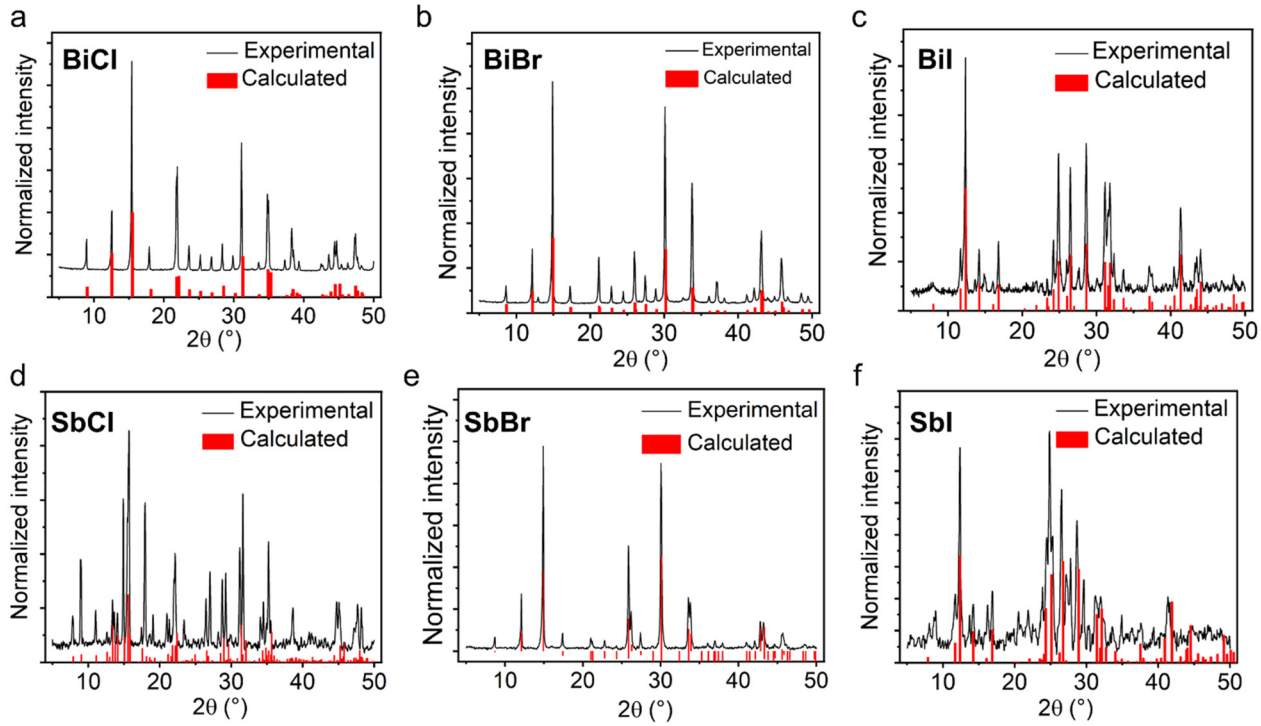

Fig. 5 PXRD patterns for **BiCl** (a), **BiBr** (b), **BiI** (c), **SbCl** (d), **SbBr** (e), and **SbI** (f).

transition from **BiBr** to **BiI** involves multiple changes: a decrease of dimensionality from 2D to 0D, a change from corner-sharing to edge-sharing connectivity of octahedra, and a change of the involved halogen orbital from 4p to 5p. While the first two effects largely offset each other, the shift to the red region primarily stems from the alteration in the halide orbital.

Considering antimony halides, at the transition from **SbCl** to **SbBr**, there is a shift from a 1D to 2D structure and a change in the involved halogen orbital from 3p to 4p. These concurrent effects lead to a redshift, and as in the case of bismuth analogues, to E_g reduction.

In contrast, the transition from **SbBr** to **SbI** involves a decrease in dimensionality from 2D to 0D, a shift from corner-sharing to edge-sharing connectivity of octahedra, and a change in the contributing halogen orbital from 4p to 5p, similar to bismuth analogues. Consequently, we would expect the E_g to appear at around 2.6 eV in line with parameters observed for Bi, however, it is found at 2.91 eV. A smaller band gap shift upon transition from Br to I can be associated with the disorder of the **SbI** crystal structure.

As for the exciton binding energy values, a clear decreasing trend across the halogen series from chloride to iodide was observed for bismuth, whereas antimony exhibited a more complex dependence. For instance, **BiBr** and **SbBr** exhibited identical exciton binding energies, along with a comparable optical band gap (Table 3). In contrast, **BiCl** showed an increased exciton binding energy of 0.61 eV, while for **SbCl** this value was the lowest for the studied series −0.06 eV. While **BiI** exhibited a binding energy of 0.12 eV, this parameter for **SbI** was 0.14 eV. The trend of exciton binding energy change does not depend linearly on the decrease of dimensionality: the lowest E_B value of 0.06 eV can be observed for 1D **SbCl**, the average values of 0.12–0.14 eV can be found for 0D **BiI** and **SbI**, while the highest E_B values of 0.47–0.61 eV are displayed by 2D **BiCl**, **BiBr** and **SbBr**. Worth noting that the presence of such intensive excitonic peaks with large binding energies are very common for Sb and Bi-based perovskite-like compounds.[46,50]

The dimensionality of the inorganic sublattice plays a pivotal role in determining the optical band gap of metal–halide perovskites. According to previous studies of halide perovskites, a general trend is an increase of the band gap with decreasing dimensionality of the $[MX_6]$ network as quantum confinement increases the separation between the valence band maximum and the conduction band minimum, thereby widening the band gap. However, this general expectation does not strictly hold in the present $(AzrH)_3M_2X_9$ series. Notably, the 2D **BiCl** compound displays a slightly larger band gap than the 1D **SbCl** analogue, despite the reduction in dimensionality. This deviation likely arises from several factors. First, the nature of the metal cation plays a key role: bismuth-based halides may exhibit larger band gaps than antimony analogues due to differences in spin–orbit coupling strength and orbital energy alignment. Second, in both **BiCl** and **SbCl** structures, the $[MX_6]$ octahedra are connected by three corners in a *fac* configuration. Thus, octahedra in **BiCl** do not share all four corners, which is more common for 2D frameworks. Such partial connectivity restricts orbital overlap

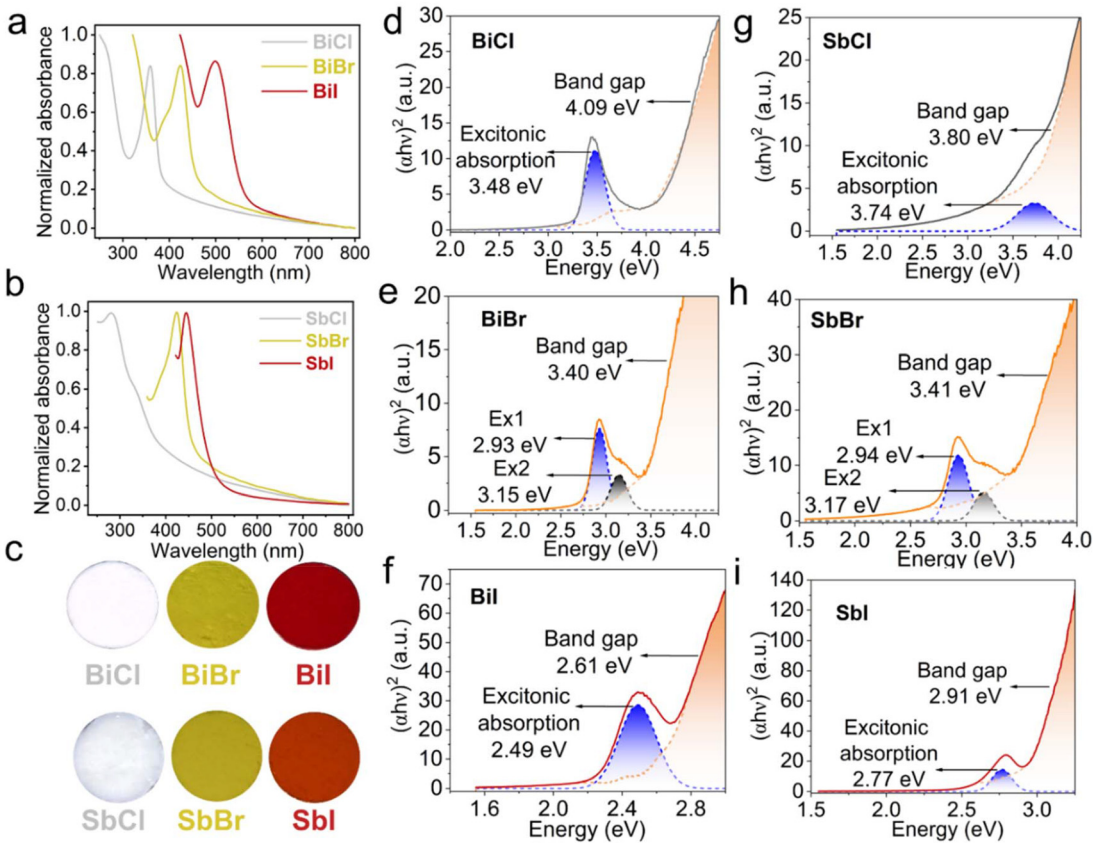

Fig. 6 (a and b) Normalized UV-vis absorbance spectra; (c) photographs of perovskite powder ($(AzrH)_3M_2Cl_9$ – white, $(AzrH)_3M_2Br_9$ – yellow, and $(AzrH)_3M_2I_9$ – red); (d–i) Tauc plots for direct band gap semiconductors. The direct bandgap semiconducting nature of the reported perovskites was confirmed by DFT calculations as shown further in the text.

Table 3 Values of E_{ex}, E_g and E_B extracted from Tauc plots

Dimensionality	Compound	E_{ex} (eV)	E_g (eV)	E_B (eV)
0D	**SbI**	2.77	2.91	0.14
	BiI	2.49	2.61	0.12
1D	**SbCl**	3.74	3.80	0.06
2D	**BiCl**	3.48	4.09	0.61
	SbBr	1st 2.94	3.41	0.47
		2nd 3.17		0.24
	BiBr	1st 2.93	3.40	0.47
		2nd 3.15		0.25
3D	$\mathbf{Bi_{0.05}Pb_{0.95}Br}$		2.23	
	$\mathbf{Bi_{0.15}Pb_{0.85}Br}$		2.18	
	$\mathbf{Bi_{0.05}Pb_{0.95}I}$		1.49	

along certain crystallographic directions, thereby diminishing the expected relationship between dimensionality and band gap reduction. Consequently, while dimensionality remains a useful framework for rationalizing band gap trends, it must be considered alongside structural details of octahedral connectivity and intrinsic cationic effects when comparing materials across different compositions and metals.

Moreover, the band gap shift from Br to I in Sb-based compounds appears less pronounced than anticipated. While a significant red-shift is expected due to the rise in halogen p-orbital energy (from 4p in Br to 5p in I), the actual band gap of **SbI** (2.91 eV) is only moderately smaller than that of **SbBr**, and significantly larger than **BiI**, despite the comparable dimensionality. This deviation can be attributed to substantial structural disorder in the **SbI** crystal, particularly involving iodine atom positions and [SbI_6] octahedral distortions. As revealed by single-crystal X-ray diffraction, all iodine atoms in **SbI** are disordered over two positions, and the resulting $Sb_2I_9^{3-}$ clusters exhibit strong angular distortion (σ^2 = 42.02° *vs.* 19.71° in **BiI**). Such disorder is known to decrease the orbital overlap between Sb and I atoms,[51] thereby limiting the extent of band dispersion and increasing the band gap.

To investigate the effect of the interplay between the structure and the composition on excitonic behavior in low-dimensional hybrid perovskites, we studied the photoluminescence (PL) properties of six obtained $(AzrH)_3M_2X_9$ compounds. Among them only three were found to display PL activity at 77 K (**BiCl**, **SbCl**, and **SbBr**; Fig. 7), while only **BiCl** was found to be luminescent at room temperature.

Meanwhile, **BiBr**, **SbI** and **SbBr** do not display PL neither at room temperature nor at 77 K.

BiCl displays strong PL both at room temperature and at 77 K, with an emission maximum at 368 nm and a full width at half maximum (FWHM) of approximately 60 nm. The small

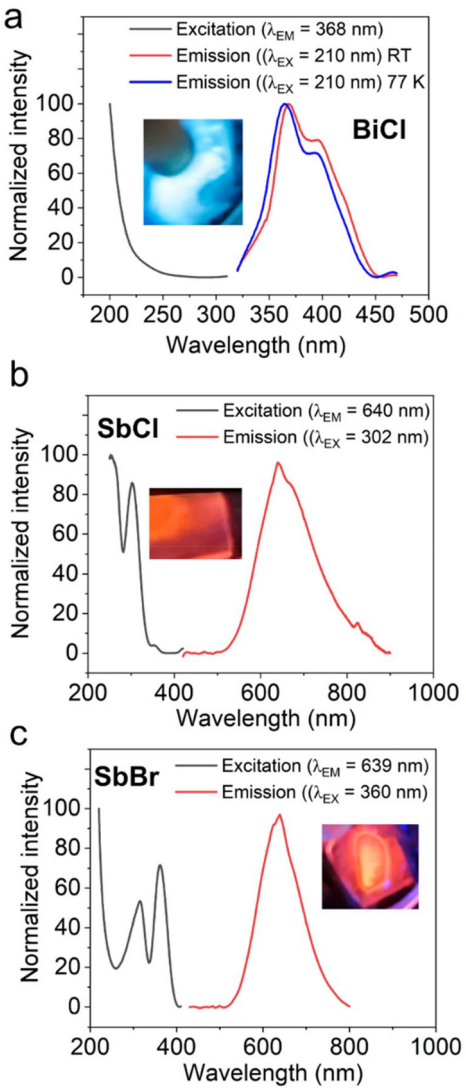

Fig. 7 PL spectra of **BiCl** (a), **SbCl** (b) and **SbBr** (c). Photographs showing luminescence of powder samples during investigation are inserted (λ_{EX} for **BiCl** is 210 nm, for **SbCl** is 302 nm, and for **SbBr** is 360 nm).

Stokes shift (~40 meV), stability of emission at elevated temperatures, and moderate spectral broadening suggest that the emission arises from free or weakly bound excitons. These excitons remain radiatively active at room temperature due to reduced self-trapping tendencies.

In contrast, **SbBr**, which is isostructural to **BiCl**, exhibits intense PL only at 77 K, with a broad emission band centred at 639 nm and a FWHM of 106 nm. The large Stokes shift (~1 eV) and broad spectral width indicate that the emission in this sample originates from self-trapped excitons (STEs). At room temperature, the PL is quenched, consistent with the thermally activated detrapping of excitons and the presence of nonradiative decay pathways.

SbCl, which has a one-dimensional (1D) chain-like structure, at 77 K exhibits a broad PL band centred at 640 nm (FWHM 135 nm), similar in shape and position to that observed in **SbBr**. This strongly suggests that the emission also arises from self-trapped excitons, stabilized by both the reduced dimensionality and the strong localization tendencies of the Sb–Cl lattice.

Taken together, these results highlight the critical role of both chemical composition and dimensionality in determining the exciton dynamics and radiative behavior in hybrid metal–halide perovskites.

In contrast to **SbCl**, **SbBr**, and **BiCl**, three additional materials—**BiBr**, **BiI**, and **SbI**—exhibited no detectable photoluminescence even at 77 K, despite their structural and compositional similarity. **BiBr** is isostructural with the luminescent **SbBr** sample and exhibits identical absorption features. Its lack of PL suggests the dominance of nonradiative recombination pathways. Compared to Sb^{3+}, the Bi^{3+} cation has stronger spin–orbit coupling, which may alter recombination dynamics and increase the likelihood of nonradiative decay.

Doping (AzrH)$PbBr_3$ and (AzrH)PbI_3 with Bi^{3+}

Mixing halogens and A-site cations in three-dimensional (3D) hybrid perovskites is well-known for tuning band gaps and enhancing stability.[44,52,53] Isovalent doping of M-site cations (M = Pb^{2+}, Sn^{2+}, and Ge^{2+}) can lead to defect passivation, band gap reduction, and increased stability,[54–57] while heterovalent doping with Bi^{3+} and Sb^{3+} significantly alters their optoelectronic properties. These dopants lower the CB bottom,[58] narrow the band gap and enhance charge carrier concentration and conductivity.[59] The introduction of Bi^{3+} and Sb^{3+} creates structural defects and defect complexes, which influence free-carrier density.[60] These changes in properties and the underlying mechanisms make Bi^{3+} and Sb^{3+} dopants valuable for enhancing perovskite-based optoelectronic devices.[61] Doping with Bi^{3+}, which has an active ns^2 lone pair, exhibits many advantageous properties. Its soft polarizability results in high Born effective charges, and strong spin–orbit coupling enhances the CB bandwidth, making it an excellent candidate for defect-tolerant compounds.[62,63]

Bi^{3+} was selected as a dopant for (AzrH)$PbBr_3$ due to its lower empty 6p orbitals compared to Pb^{2+}. This substitution alters the electronic structure[64] of 3D (AzrH)PbX_3, enhancing its potential for optoelectronic devices. We doped (AzrH)$PbBr_3$ and (AzrH)PbI_3 with 5% and 15% Bi^{3+} to investigate the dependence of the band gap on the amount of bismuth. Both bromide samples maintain their 3D structure (Fig. 8), according to PXRD analysis. The iodide samples conserve the 3D structure in the case of 5% doping, while at 15% doping an extra phase is formed (see Fig. S2†). Rietveld refinement was performed in order to study the influence of Bi-doping on the cubic structure and confirm the phase purity (Fig. S3 and Table S3†). The refinement revealed that there is almost no change in the lattice parameter (5.97 Å for (AzrH)$PbBr_3$ and 5.99 Å for both Bi-doped samples) of the cubic hybrid perovskite upon bismuth incorporation. Such a behavior was expected due to the tendency of bismuth to form a 2D structure which mimics the 3D perovskite framework and does not

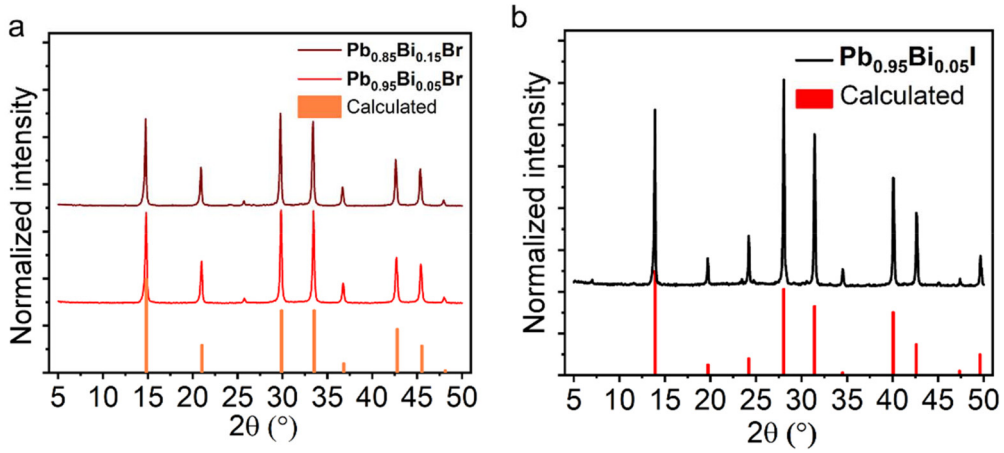

Fig. 8 (a) Calculated PXRD pattern of $(AzrH)PbBr_3$ (orange) and experimental PXRD patterns of Bi^{3+}-doped $(AzrH)PbBr_3$: red and dark-red lines stand for 5 and 15% doping, respectively. (b) Calculated PXRD pattern of $(AzrH)PbI_3$ (red) and the experimental PXRD pattern of $(AzrH)PbI_3$ doped with 5% of Bi^{3+} (black).

cause a disruption in bromide lead perovskite. The ICP analysis showed that the bismuth content in the obtained doped perovskite is somewhat lower than in precursor solutions (Table S4†). It is worth noting that in the case of $(AzrH)PbBr_3$ heterovalent doping with Bi^{3+} the reduction of the lead content is not fully compensated by the equal increase of the bismuth content, indicating that the charge balance is maintained through the creation of lead vacancies.

In contrast, doping aziridinium lead iodide with bismuth results in more significant distortion of the 3D lattice due to the 0D structure of bismuth-based metal halide. To evaluate the semiconducting properties, we measured UV-vis absorbance and analyzed the data using the Tauc plot (Fig. 9). Doping $(AzrH)PbBr_3$ with 5% Bi^{3+} shifted the band gap from 2.24 eV (undoped) to 2.23 eV. Increasing the Bi^{3+} content to 15% further decreased the band gap to 2.18 eV. Similarly,

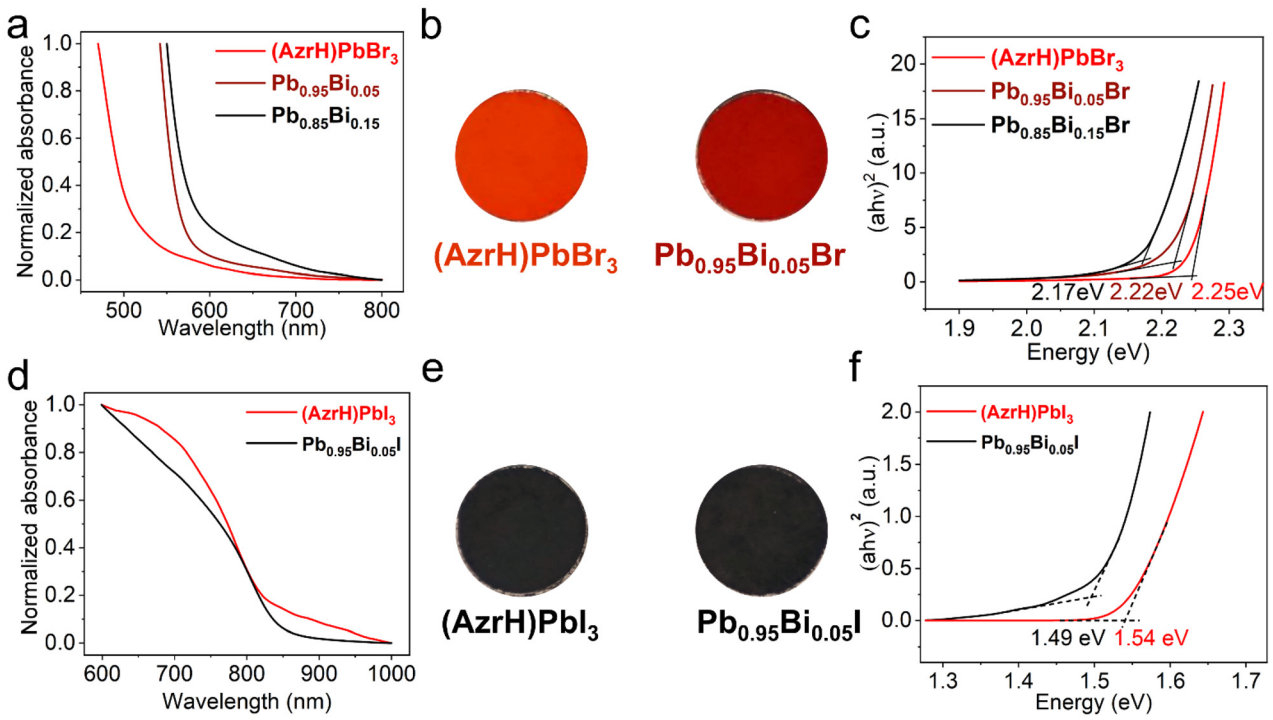

Fig. 9 (a and d) Normalized UV-vis absorbance spectra of undoped $(AzrH)PbBr_3$ and $(AzrH)PbI_3$ along with the spectra of the corresponding perovskites doped with Bi^3; (b and e) photographs of undoped and doped perovskite bulk samples; and (c and f) Tauc plots for undoped and Bi^{3+}-doped $(AzrH)PbBr_3$ and $(AzrH)PbI_3$ calculated for direct bandgap semiconductors.

doping (AzrH)PbI_3 with 5% Bi^{3+} shifted the band gap from 1.54 eV to 1.49 eV. Very similar behaviour of band gap reduction with lattice parameter conservation has been previously observed for Bi-doped $MAPbBr_3$.[59,65]

Doping of (AzrH)$PbBr_3$ and (AzrH)PbI_3 with Sb instead of Bi revealed very similar results. While Sb-doped (AzrH)$PbBr_3$ retains its cubic structure upon both 5% and 15% Sb incorporation, in the case of (AzrH)PbI_3 the cubic structure is conserved only at 5% Sb-doping (Fig. S4 and S5†). Doping (AzrH)PbI_3 with 15% of Sb leads to the formation of some additional phases. The band gap values of (AzrH)$PbBr_3$ also undergo a red shift upon Sb-doping and are observed at 2.23 and 2.20 eV for **$Pb_{0.95}Sb_{0.05}Br$** and **$Pb_{0.85}Sb_{0.15}Br$**, respectively. As for (AzrH)PbI_3, its doping with 5% of Sb leads to a decrease in the BG value to 1.52 eV.

Interestingly, the inverse doping of $A_3B_2X_9$ metal halide by the B^{2+} cation has also been reported, further demonstrating the versatility and potential of this approach in tuning the properties of perovskite materials.[39]

DFT calculations

Density functional theory (DFT) calculations were used to investigate the electronic properties of the newly synthesized $(AzrH)_3M_2X_9$ hybrid perovskites. We performed the calculations using the semi-local exchange–correlation functional, specifically the Generalized Gradient Approximation (GGA) of the Perdew–Burke–Ernzerhof (PBE) functional.[66] To achieve high accuracy, we utilized the triple-zeta basis set for the potential model.

The band structure of the hybrid perovskites was computed along the high-symmetry points of the Brillouin zone. The energy range is depicted from −3.5 eV to 3.5 eV, with the Fermi level set at 0 eV. The CB and valence bands (VB) are well-defined, confirming the semiconducting nature of the calculated structures. Partial density of states (PDOS) calculations were performed to identify the contributions of various atomic orbitals to the electronic states. The PDOS results indicate that the electronic states are primarily influenced by the p-orbitals of the halogen and metal atoms.

In **BiCl**, the conduction band minimum (CBM) and the valence band maximum (VBM) are located along the Γ point (Fig. 10(a, c and e)). The calculated direct band gap is 3.36 eV in comparison with 4.09 eV obtained in optical measurements. The lower values of calculated E_g in comparison with the experiment are expected, when the PBE functional is applied, it is known that such functionals can systematically underestimate the band gap values due to self-interaction error.[66] The band structure of **BiCl** is relatively dispersive. This observation may indicate strong intralayer coupling in this 2D perovskite. According to PDOS, the VBM (−2.00 eV) has the major contribution from Cl p-orbitals. The CBM (1.36 eV) is primarily defined by Bi p-orbitals, with a smaller contribution from the halogen (Fig. 10e).

In **SbCl**, the band edge extremes are located along the T direction, revealing a direct band gap value of 2.91 eV, which is lower than the optical band gap of 3.80 eV. The less dispersive band structure of **SbCl** can be attributed to its reduced dimensionality compared to **BiCl** (1D *versus* 2D).[67] The PDOS for **SbCl** reveals a density nearly four times higher than **BiCl**,

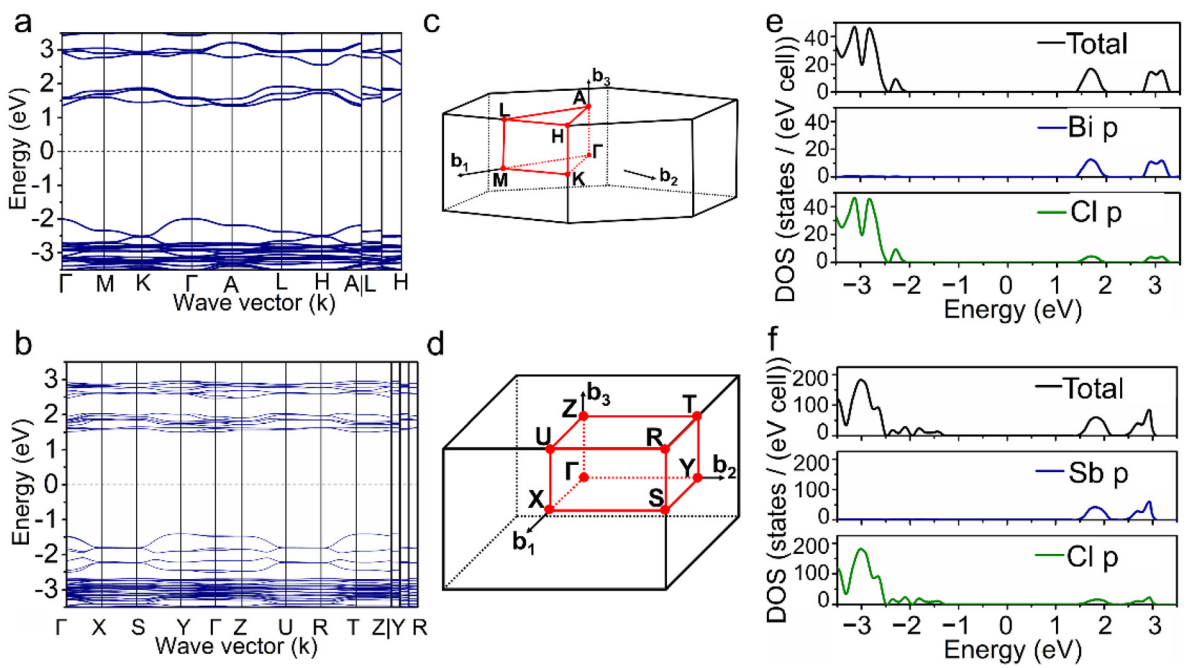

Fig. 10 (a and b) Calculated band structures of **BiCl** and **SbCl**, respectively; (c) Brillouin zone for hexagonal cell showing high-symmetry points (path: Γ–M–K–Γ–A–L–H–A|L–M|K–H) and (d) Brillouin zone for orthorhombic cell showing high-symmetry points (path Γ–X–S–Y–Γ–Z–U–R–T–Z|Y–T|U–X|S–R); and (e and f) the calculated partial and total density of states for **BiCl** and **SbCl**, respectively.

consistent with their unit cell volume ratio. VBM, which is found at −1.41 eV is primarily determined by chlorine p-orbitals.

The CB (with CBM of 1.50 eV) has a higher contribution from Sb p-orbitals compared to the halogen.

The band structures of **MBr** exhibit similarities (Fig. 11), with both the VBM and CBM located along the Γ direction. The VBM is found at −1.64 eV and −0.89 eV below the Fermi level, for **BiBr** and **SbBr**, respectively, while the CBM can be found at 1.09 and 1.28 eV for **BiBr** and **SbBr**, respectively. A notable distinction is observed in the greater band splitting for **SbBr**, resulting in a significantly underestimated band gap of 2.17 eV compared to the 3.41 eV obtained from UV-vis absorbance spectra. In contrast, **BiBr** shows a calculated band gap of 2.73 eV compared to the measured value of 3.40 eV. Given that these compounds have nearly identical lattice parameters, their PDOS are also similar. The PDOS displays numerous overlapping band sets in the VB, predominantly determined by bromide p-orbitals. The CB is nearly identical as well, with significant contributions from the metal p-orbitals.

As previously mentioned, a decrease in dimensionality reduces band dispersion, which is evident in the 0D **BiI** bands (Fig. 12). **BiI** is characterized by the flattest bands in the VB, with a weakly expressed VBM (−1.12 eV) along the A direction, indicating heavy holes with large effective masses.[68] The set of overlapping bands extends from 3 eV to 1 eV below the Fermi level. As for the CB, its minimum is located in the A direction at 1.16 eV. This highlights a direct band gap of 2.28 eV, which is lower than the experimentally obtained band gap of 2.61 eV. The PDOS reveals similar results, with the VB primarily determined by the p-orbitals of the halogen, while the CB remains mainly influenced by the p-orbitals of the metal.

Due to the disordered crystal structure of **SbI**, iodine atoms were randomly selected for modeling. Similar to **BiI**, **SbI** exhibits a less dispersed band distribution in comparison with other halides. The band splitting in **SbI** is stronger than in bismuth-based compounds, a similar observation was made for bromide perovskites described here. The VB edge maximum is located along the M direction at −1.72 eV relative to the Fermi level, and the CBM lies at 0.42 eV. Thus, **SbI** is characterized by a direct band gap of 2.14 eV.

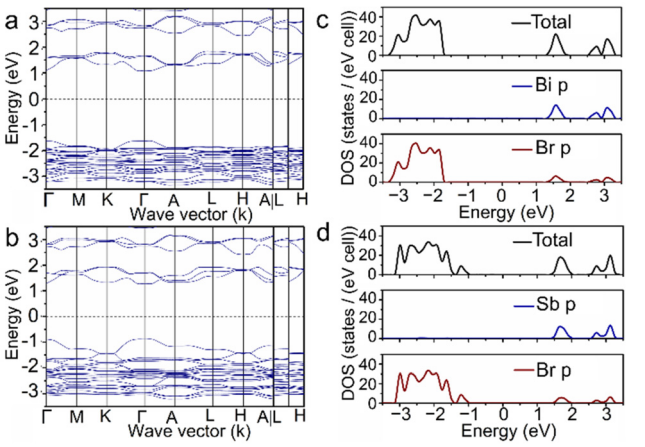

Fig. 11 (a and b) Calculated band structures of **BiBr** and **SbBr**, respectively and (c and d) the calculated density of states for **BiBr** and **SbBr**, respectively (only orbitals with significant contributions are shown).

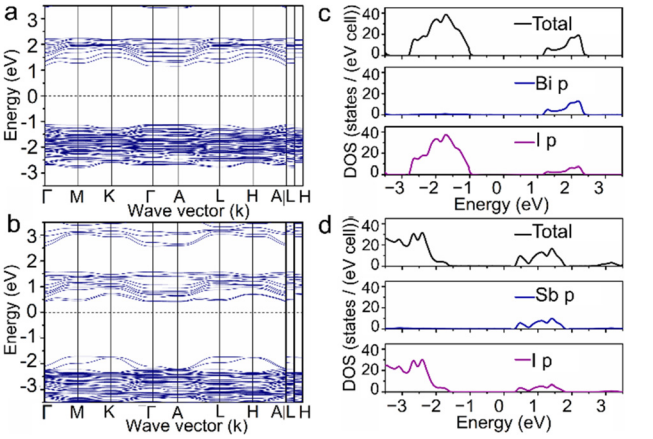

Fig. 12 (a and b) Calculated band structures of **BiI** and **SbI**, respectively and (c and d) the calculated density of states for **BiI** and **SbI**, respectively (only orbitals with significant contributions are shown).

Additionally, we performed DFT calculations for the crystal structure of **SbI** modeled without disorder which results in higher anisotropy (Fig. S6†). The band structure of this ordered model shows a more reasonable position of the VBM (−1.07 eV) and CBM (1.16 eV). The band gap values in the ordered model are slightly higher. The lowest energy of the indirect transition is 2.23 eV, occurring from K to A points. The PDOS for the non-disordered model shows lower band overlapping and a higher density of states in the CB. PDOS for both models reveals that the VB is primarily determined by the p-orbitals of the halogen, while the CB is mainly influenced by the p-orbitals of the metal.

In order to characterize the Bi-doping effect on $(AzrH)PbBr_3$ perovskite computationally, we have performed DFT calculations of the band structure and density of states for two super cells: one containing 8 lead ions (Fig. 13(a)) and the second one containing 5 lead ions, 2 bismuth ions and one lead vacancy (Fig. 13(b)). The band structure for the super cell of $(AzrH)PbBr_3$ demonstrates the presence of a direct band gap of 1.65 eV along the Γ direction (Fig. 13(c)). This calculation using supercell corroborates well with calculations for a simple cell performed by us previously.[69] The location of the bandgap depends on the change of the lead position in the cell used for calculations, which is located at the Γ symmetry point in the super cell and at the R point when one unit cell is used for calculations. The direct band gap often appears at the high-symmetry point in reciprocal space that reflects the strongest periodic potential modulations created by the arrangement of heavy atoms—in this case, lead. When the arrangement of lead atoms changes between models, the corresponding symmetry points and their contributions to the band structure

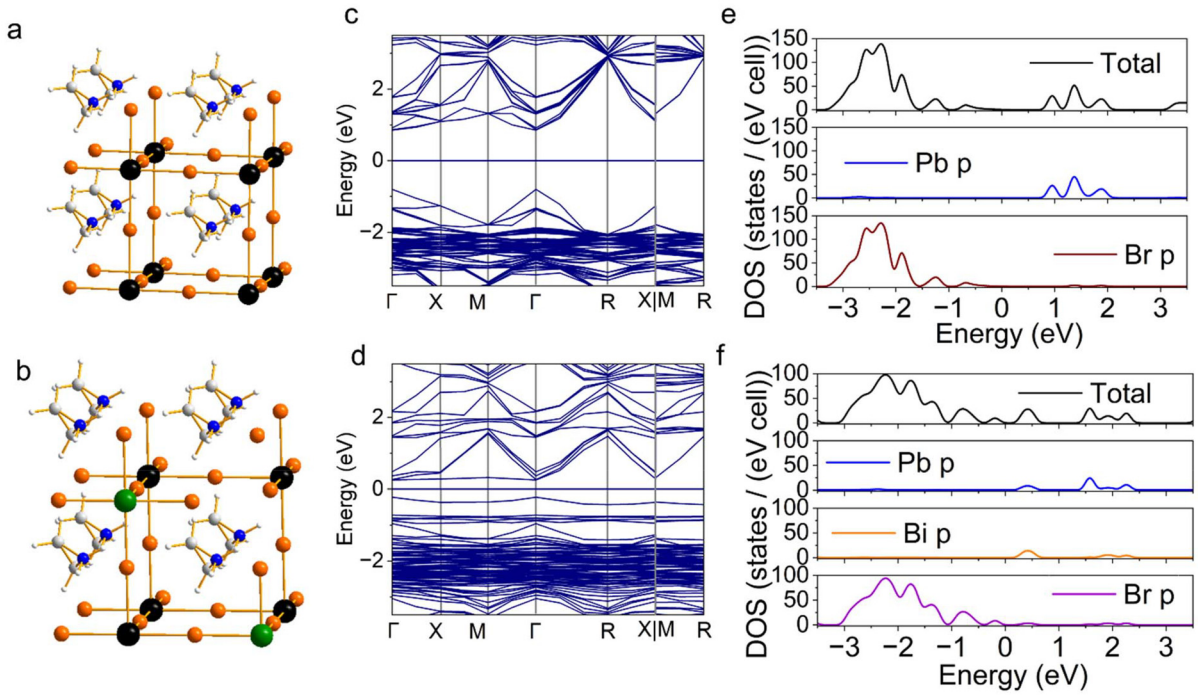

Fig. 13 Demonstration of super cells used for DFT calculations of (AzrH)$PbBr_3$ (a) and Bi-doped (AzrH)$PbBr_3$ (b). (c and d) Calculated band structures of (AzrH)$PbBr_3$ and Bi-doped (AzrH)$PbBr_3$, respectively; and (e and f) calculated density of states for (AzrH)$PbBr_3$ and Bi-doped (AzrH)$PbBr_3$, respectively (only orbitals with significant contributions are shown).

also shift, leading to the observed difference. According to PDOS, the VBM (−0.80 eV) in the super cell of (AzrH)$PbBr_3$ has the major contribution from Br p-orbitals. CBM (0.85 eV) is primarily defined by Pb p-orbitals, with a smaller contribution from the halogen.

The introduction of bismuth ions and lead defects leads to a significant decrease in the direct band gap along the Γ direction down to 0.47 eV. Simultaneously, bismuth doping leads to a significant flattening of bands, especially pronounced in the valence band, which is indicated by the presence of heavy holes with larger effective masses and lower carrier mobility in comparison with (AzrH)$PbBr_3$ which is characterized by a more dispersive band structure. According to PDOS, the VBM (−0.22 eV) in the super cell of Bi-doped (AzrH)$PbBr_3$ has the major contribution from Br p-orbitals. The CBM (0.25 eV) is primarily defined by Pb and Bi p-orbitals, with a smaller contribution from the halogen.

In general, the application of the PBE exchange–correlation functional, while computationally efficient, is known to systematically underestimate the band gap values in semiconductors and perovskite-like materials due to its self-interaction error and lack of exact exchange. This underestimation is particularly pronounced in systems containing heavy elements such as bismuth and iodine, where relativistic effects, especially spin–orbit coupling (SOC), play a critical role in determining the electronic structure. SOC strongly affects the energy levels of the conduction band, primarily formed from Bi 6p orbitals, by splitting and shifting them downward, and effectively narrowing the band gap.

Beyond mere energy shifts, SOC also modifies the band curvature and effective masses of carriers. SOC alters the orbital character near the band edges by mixing states and changing band ordering, often lifting degeneracies at high-symmetry points. This can reduce band dispersion and result in anisotropic transport behavior. In the context of hybrid perovskites, such effects are especially significant in 0D and 2D structures where confinement already restricts delocalization.

Experimental

All the synthetic procedures are described in detail in the ESI.†

Spectroscopy

FTIR spectra were recorded with a PerkinElmer spectrometer BX II (4000–600 cm^{-1}) in the ATR mode (Fig. S7 and Table S5†).

All UV-Vis spectra were recorded on a Varian Cary 50 UV-vis spectrophotometer in the transmission mode in a range from 250 to 800 nm with a scan rate of 60.000 (nm min^{-1}).

PL spectra were acquired using a Shimadzu RF-6000 spectrofluorometer. Temperature was controlled using a DSC 600 cryostage. The sample chamber was purged with dry nitrogen prior to cooling to avoid water condensation. Spectra were acquired at 77 K and at room temperature.

Crystallography

Single-crystal X-ray diffraction data were acquired using an Oxford-Diffraction XCALIBUR Eos CCD diffractometer (**BiI**,

BiBr, and **SbI**) or a Rigaku XtaLAB Synergy Dualflex HyPix diffractometer (**BiCl**, **SbCl**, and **SbI**), utilizing graphite-monochromated Mo-Kα radiation. The unit cell parameters and data integration were handled using the CrysAlisPro software suite from Oxford Diffraction. Structural solutions were obtained using the ShelXT program with intrinsic phasing, and further refined using the full-matrix least squares method on F^2 using ShelXL. The Olex2 software was used as the interface for the ShelX programs. In all structural models, metal and halogen atoms were refined anisotropically. For all structures except **SbCl**, the C and N atoms of the disordered aziridinium cation were refined isotropically with a restrained C–N bond distance of 1.45 Å. In the **SbCl** structure, hydrogen atoms were placed at calculated positions with $U_{iso}(H) = 1.2U_{eq}(C,N)$. The hydrogen atoms of the CH_2 group were positioned with a C–H bond length of 0.99 Å.

The crystallographic data of the structures described in this paper were deposited at the Cambridge Crystallographic Data Center (CCDC 2448195–2448200†).

The PXRD patterns were acquired on a Shimadzu XRD-6000 diffractometer using Cu-Kα radiation (5–50° range, 0.05° step). The model for Bi- and Sb-doped samples was refined using GSAS II[70] by the Rietveld refinement method. The Chebyschev function with 3 terms was used to fit the background. The PseudoVoigt function was used to model the peak shape. Pb, Br and Bi/Sb atoms were refined as anisotropic, C and N as isotropic.

ICP of Bi- and Sb-doped samples was measured using an Analytik Jena ICP-OES PlasmaQuant PQ 9000. Solutions used for measurements contained 10 mg of doped perovskites, 2 ml of HNO_3 conc. (68%) and distilled water to reach the total volume of 50 ml.

Calculations

The band structure and density of states (DOS) were computed using the crystal structure refined from single-crystal diffraction data. Density functional theory (DFT) calculations were conducted using AMS BAND software without further atomic coordinate optimization.[71,72] The total energy calculations were based on DFT with the Perdew–Burke–Ernzerhof (PBE) generalized gradient approximation (GGA). A *k*-point mesh of 3 × 3 × 3 was employed for **MCl** and **MBr**, and 3 × 3 × 1 for **MI**, because of the elongated unit cell. The basis set included triple-zeta with one polarization function. Scalar relativistic effects were incorporated using the ZORA approach.[73,74]

Conclusions

In summary, we have successfully synthesised and characterised six new low-dimensional perovskite-like metal halides with the general formula $(AzrH)_3M_2X_9$ ((AzrH) = aziridinium, M = Sb, Bi; X = Cl, Br, and I). The single crystal X-ray diffraction study revealed that $(AzrH)_3Sb_2Cl_9$ crystallizes as 1D double-chains in the non-centrosymmetric space group $P2_12_12_1$. The polar nature of this space group indicates that this hybrid material could be investigated for potential ferroelectric properties. $(AzrH)_3Bi_2Cl_9$, $(AzrH)_3Bi_2Br_9$ and $(AzrH)_3Sb_2Br_9$ crystallize in the $P\bar{3}m1$ space group. These compounds form 2D layers which mimic an AMX_3 3D structure that misses every third layer of B-site cations. $(AzrH)_3Bi_2I_9$ and $(AzrH)_3Sb_2I_9$ crystallize in the $P6_3/mmc$ space group forming discrete 0D face-sharing octahedra. Notably, $(AzrH)_3Sb_2I_9$ exhibits disorder with two possible positions for each iodide, which significantly affects optical and electronic properties.

Comprehensive analysis of the crystal structure shows how dimensionality affects the width of the optical band gap and exciton binding energy. The obtained band gap values are 2.61 eV, 3.40 eV, and 4.09 eV for $(AzrH)_3Bi_2I_9$, $(AzrH)_3Bi_2Br_9$, and $(AzrH)_3Bi_2Cl_9$, respectively, and 2.91 eV, 3.41 eV, and 3.80 eV for $(AzrH)_3Sb_2I_9$, $(AzrH)_3Sb_2Br_9$, and $(AzrH)_3Sb_2Cl_9$, respectively. Moreover, the reported structures possess strong excitonic peaks with the maximum in the range of 330–499 nm and exciton binding energy ranging from 0.06 eV to 0.61 eV.

For the first time, we have demonstrated heterovalent doping of aziridinium-based perovskites. By doping both $(AzrH)PbBr_3$ and $(AzrH)PbI_3$ with 5% and/or 15% bismuth, we achieved a reduction in the band gap from 2.24 eV to 2.18 eV and from 1.54 to 1.49 eV, respectively. Phase analysis reveals that increasing the dimensionality of the dopant promotes the possibility of supporting a 3D framework.

Electronic properties were studied by DFT calculations. Calculated band structures show the dependence of band dispersion on dimensionality. Partial density of states calculations reveal that the valence band of all studied perovskites is predominantly determined by p-orbitals of halogens, while the conduction band is mainly affected by p-orbitals of metals with a lower contribution of halogens.

Our findings lay a robust foundation for further exploration into the design and synthesis of novel perovskite-like materials with tailored properties, potentially revolutionizing fields such as photovoltaics, light-emitting diodes, and ferroelectric devices.

Author contributions

Olesia I. Kucheriv: writing – original draft and formal analysis; Oleksandr A. Semenikhin: writing – original draft, investigation, and formal analysis; Yurii S. Bibik: investigation; Ivan Bardyk: investigation; Sergiu Shova: investigation and formal analysis; Il'ya A. Gural'skiy: supervision, conceptualization, funding acquisition, and writing – review & editing.

Conflicts of interest

There are no conflicts to declare.

Data availability

The data supporting this article have been included as part of the ESI.† Crystallographic data for **SbCl**, **SbBr**, **SbI**, **BiCl**, **BiBr**

and **BiI** have been deposited at the Cambridge Crystallographic Data Center under CCDC numbers 2448195–2448200† and can be obtained from **https://www.ccdc.cam.ac.uk/**.

Acknowledgements

Funding for this research was provided by the EURIZON project, which is funded by the European Union (grant no. 871072), and the Ministry of Education and Science of Ukraine (grant no. 24BF037-02). The author(s) are grateful to the FAIRE programme provided by the Cambridge Crystallographic Data Centre (CCDC) for the opportunity to use the Cambridge Structural Database (CSD) and associated software. The support from AMS is acknowledged. The authors also acknowledge the courage of all the brave defenders of Ukraine who made the submission of this manuscript possible.

References

1 Y. Zhao and K. Zhu, Organic–Inorganic Hybrid Lead Halide Perovskites for Optoelectronic and Electronic Applications, *Chem. Soc. Rev.*, 2016, **45**, 655–689.
2 X.-K. Liu, W. Xu, S. Bai, Y. Jin, J. Wang, R. H. Friend and F. Gao, Metal Halide Perovskites for Light-Emitting Diodes, *Nat. Mater.*, 2021, **20**, 10–21.
3 Y. Hassan, J. H. Park, M. L. Crawford, A. Sadhanala, J. Lee, J. C. Sadighian, E. Mosconi, R. Shivanna, E. Radicchi, M. Jeong, C. Yang, H. Choi, S. H. Park, M. H. Song, F. De Angelis, C. Y. Wong, R. H. Friend, B. R. Lee and H. J. Snaith, Ligand-Engineered Bandgap Stability in Mixed-Halide Perovskite LEDs, *Nature*, 2021, **591**, 72–77.
4 J. J. Yoo, G. Seo, M. R. Chua, T. G. Park, Y. Lu, F. Rotermund, Y. Kim, C. S. Moon, N. J. Jeon, J.-P. Correa-Baena, V. Bulović, S. S. Shin, M. G. Bawendi and J. Seo, Efficient Perovskite Solar Cells via Improved Carrier Management, *Nature*, 2021, **590**, 587–593.
5 L. Zhou, J. Liao and D. Kuang, An Overview for Zero–Dimensional Broadband Emissive Metal–Halide Single Crystals, *Adv. Opt. Mater.*, 2021, **9**, 2100544.
6 Q. Wang, Q. Zhou, M. Nikl, J. Xiao, R. Kucerkova, A. Beitlerova, V. Babin, P. Prusa, V. Linhart, J. Wang, X. Wen, G. Niu, J. Tang, G. Ren and Y. Wu, Highly Resolved X–Ray Imaging Enabled by In(I) Doped Perovskite–Like $Cs_3Cu_2I_5$ Single Crystal Scintillator, *Adv. Opt. Mater.*, 2022, **10**, 2200304.
7 M. Z. Rahaman, S. Ge, C.-H. Lin, Y. Cui and T. Wu, One–Dimensional Molecular Metal Halide Materials: Structures, Properties, *Small Struct.*, 2021, **2**, 2000062.
8 X. Song, H. Yin, Q. Chang, Y. Qian, C. Lyu, H. Min, X. Zong, C. Liu, Y. Fang, Z. Cheng, T. Qin, W. Huang and L. Wang, One-Dimensional $(NH{=}ClNH_3)_3PbI_5$ Perovskite for Ultralow Power Consumption Resistive Memory, *Research*, 2021, **2021**, 9760729.
9 X. T. Li, J. M. Hoffman and M. G. Kanatzidis, The 2D Halide Perovskite Rulebook: How the Spacer Influences Everything from the Structure to Optoelectronic Device Efficiency, *Chem. Rev.*, 2021, **121**, 2230–2291.
10 Akriti, E. Shi, S. B. Shiring, J. Yang, C. L. Atencio-Martinez, B. Yuan, X. Hu, Y. Gao, B. P. Finkenauer, A. J. Pistone, Y. Yu, P. Liao, B. M. Savoie and L. Dou, ayer-by-Layer Anionic Diffusion in Two-Dimensional Halide Perovskite Vertical Heterostructures, *Nat. Nanotechnol.*, 2021, **16**, 584–591.
11 B. Saparov and D. B. Mitzi, Organic–Inorganic Perovskites: Structural Versatility for Functional Materials Design, *Chem. Rev.*, 2016, **116**, 4558–4596.
12 I. Metcalf, S. Sidhik, H. Zhang, A. Agrawal, J. Persaud, J. Hou, J. Even and A. D. Mohite, Synergy of 3D and 2D Perovskites for Durable, Efficient Solar Cells and Beyond, *Chem. Rev.*, 2023, **123**, 9565–9652.
13 V. Trifiletti, S. Luong, G. Tseberlidis, S. Riva, E. S. S. Galindez, W. P. Gillin, S. Binetti and O. Fenwick, wo-Step Synthesis of Bismuth-Based Hybrid Halide Perovskite Thin-Films, *Materials*, 2021, **14**, 7827.
14 S. T. Thornton, G. Abdelmageed, R. F. Kahwagi and G. I. Koleilat, Progress towards Lead-Free, Efficient, and Stable Perovskite Solar Cells, *J. Chem. Technol. Biotechnol.*, 2022, **97**, 810–829.
15 V.-H. Vuong, S. V. N. Pammi, S. Ippili, V. Jella, T. Nguyen Thi, K. Sairam Pasupuleti, M.-D. Kim, M. Ji Jeong, J.-R. Jeong, H. Sik Chang and S.-G. Yoon, Flexible, Stable, and Self-Powered Photodetectors Embedded with Chemical Vapor Deposited Lead-Free Bismuth Mixed Halide Perovskite Films, *Chem. Eng. J.*, 2023, **458**, 141473.
16 S. Dong, D. Xin, M. Zhang, S. Tie, B. Cai, Q. Ma and X. Zheng, Green Solvent Blade-Coated $MA_3Bi_2I_9$ for Direct-Conversion X-Ray Detectors, *J. Mater. Chem. C*, 2022, **10**, 6236–6242.
17 N. K. Tailor, S. Mishra, T. Sharma, A. K. De and S. Satapathi, Cation-Dependent Hot Carrier Cooling in the Lead-Free Bismuth Halide $A_3Bi_2I_9$ (A = FA, MA, and Cs) Perovskite, *J. Phys. Chem. C*, 2021, **125**, 9891–9898.
18 E. Jedlicka, J. Wang, J. Mutch, Y.-K. Jung, P. Went, J. Mohammed, M. Ziffer, R. Giridharagopal, A. Walsh, J.-H. Chu and D. S. Ginger, Bismuth Doping Alters Structural Phase Transitions in Methylammonium Lead Tribromide Single Crystals, *J. Phys. Chem. Lett.*, 2021, **12**, 2749–2755.
19 J. Marí-Guaita, A. Bouich and B. Marí, Stability Improvement of Methylammonium Lead Iodide Perovskite Thin Films by Bismuth Doping, *JOM*, 2022, **74**, 3103–3110.
20 I. K. Popoola, M. A. Gondal, A. Popoola and L. E. Oloore, Bismuth-Based Organometallic-Halide Perovskite Photo-Supercapacitor Utilizing Novel Polymer Gel Electrolyte for Hybrid Energy Harvesting and Storage Applications, *J. Energy Storage*, 2022, **53**, 105167.
21 J.-Q. Zhao, M.-F. Han, X.-J. Zhao, Y.-Y. Ma, C.-Q. Jing, H.-M. Pan, D.-Y. Li, C.-Y. Yue and X.-W. Lei, Structural Dimensionality Modulation toward Enhanced

Photoluminescence Efficiencies of Hybrid Lead-Free Antimony Halides, *Adv. Opt. Mater.*, 2021, **9**, 2100556.

22 M. Roknuzzaman, J. A. Alarco, H. Wang and K. (Ken) Ostrikov, Electronic and Optical Properties of Lead-Free Antimony-Copper Based Hybrid Double Perovskites for Photovoltaics and Optoelectronics by First Principles Calculations, *Comput. Mater. Sci.*, 2021, **186**, 110009.

23 J. Li, Y. Sang, L. Xu, H. Lu, J. Wang and Z. Chen, Highly Efficient Light–Emitting Diodes Based on an Organic Antimony(III) Halide Hybrid, *Angew. Chem., Int. Ed.*, 2022, **61**, e202113450.

24 U. Farooq, M. Ishaq, U. A. Shah, S. Chen, Z.-H. Zheng, M. Azam, Z.-H. Su, R. Tang, P. Fan, Y. Bai and G.-X. Liang, Bandgap Engineering of Lead-Free Ternary Halide Perovskites for Photovoltaics and beyond: Recent Progress and Future Prospects, *Nano Energy*, 2022, **92**, 106710.

25 Q. Ba, J. Kim, H. Im, S. Lin and A. Jana, Modulation of the Optical Bandgap and Photoluminescence Quantum Yield in Pnictogen (Sb^{3+}/Bi^{3+})-Doped Organic–Inorganic Tin(IV) Perovskite Single Crystals and Nanocrystals, *J. Colloid Interface Sci.*, 2022, **606**, 808–816.

26 H. Peng, Y. Tian, X. Wang, T. Huang, Y. Xiao, T. Dong, J. Hu, J. Wang and B. Zou, Bulk Assembly of a 0D Organic Antimony Chloride Hybrid with Highly Efficient Orange Dual Emission by Self-Trapped States, *J. Mater. Chem. C*, 2021, **9**, 12184–12190.

27 S. K. Shil, F. Wang, Z. Lai, Y. Meng, Y. Wang, D. Zhao, M. K. Hossain, K. O. Egbo, Y. Wang, K. M. Yu and J. C. Ho, Crystalline All-Inorganic Lead-Free Cs3Sb2I9 Perovskite Microplates with Ultra-Fast Photoconductive Response and Robust Thermal Stability, *Nano Res.*, 2021, **14**, 4116–4124.

28 J. Wu, X. Li, X. Lian, B. Su, J. Pang, M.-D. Li, Z. Xia, J. Z. Zhang, B. Luo and X.-C. Huang, Ultrafast Study of Exciton Transfer in Sb(III)-Doped Two-Dimensional $[NH_3(CH_2)_4NH_3]CdBr_4$ Perovskite, *ACS Nano*, 2021, **15**, 15354–15361.

29 H. R. Petrosova, O. I. Kucheriv, S. Shova and I. A. Gural'skiy, Aziridinium Cation Templating 3D Lead Halide Hybrid Perovskites, *Chem. Commun.*, 2022, **58**, 5745–5748.

30 O. I. Kucheriv, V. Y. Sirenko, H. R. Petrosova, V. A. Pavlenko, S. Shova and I. A. Gural'skiy, Lead-Free 3D Hybrid Perovskites Based on an Aziridinium Cation, *Inorg. Chem. Front.*, 2023, **10**, 6953–6963.

31 S. V. Kun, V. B. Lazarev, E. Y. Peresh, A. V. Kun and Y. V. Voroshilov, Phase Equilibria in RbBr-Sb(Bi)Br3 Systems and Crystal Structure of Compounds of $A_{31}B_{25}C_{97}$ (A1 - Rb, Cs; B5 -Sb, Bi; C7 - Br, I) Type, *Neorg. Mater.*, 1993, **29**, 410–413.

32 H. Ishihara, K. Watanabe, A. Iwata, K. Yamada, Y. Kinoshita, T. Okuda, V. G. Krishnan, S. Dou and A. Weiss, NQR and X-Ray Studies of $[N(CH_3)_4]_3M_2X_9$ and $(CH_3NH_3)_3M_2X_9$ (M = Sb,Bi; X = Cl,Br), *Z. Naturforsch. A*, 1992, **47**, 65–74.

33 K. Mencel, P. Starynowicz, M. Siczek, A. Piecha-Bisiorek, R. Jakubas and W. Medycki, Symmetry Breaking Structural Phase Transitions, Dielectric Properties and Molecular Motions of Formamidinium Cations in 1D and 2D Hybrid Compounds: $(NH_2CHNH_2)_3[Bi_2Cl_9]$ and $(NH_2CHNH_2)_3[Bi_2Br_9]$, *Dalton Trans.*, 2019, **48**, 14829–14838.

34 B. Chabot and E. Parthé, $Cs_3Sb_2I_9$ and $Cs_3Bi_2I_9$ with the Hexagonal $Cs_3Cr_2Cl_9$ Structure Type, *Acta Crystallogr., Sect. B*, 1978, **34**, 645–648.

35 Y. Dang, Y. Zhou, X. Liu, D. Ju, S. Xia, H. Xia and X. Tao, Formation of Hybrid Perovskite Tin Iodide Single Crystals by Top–Seeded Solution Growth, *Angew. Chem., Int. Ed.*, 2016, **55**, 3447–3450.

36 M. Luan, J. Song, X. Wei, F. Chen and J. Liu, Controllable Growth of Bulk Cubic-Phase $CH_3NH_3PbI_3$ Single Crystal with Exciting Room-Temperature Stability, *CrystEngComm*, 2016, **18**, 5257–5261.

37 Y. Takahashi, R. Obara, Z. Z. Lin, Y. Takahashi, T. Naito, T. Inabe, S. Ishibashi and K. Terakura, Charge-Transport in Tin-Iodide Perovskite $CH_3NH_3SnI_3$: Origin of High Conductivity, *Dalton Trans.*, 2011, **40**, 5563–5568.

38 H. Wang, H. Wu, Y. Xian, G. Niu, W. Yuan, H. Li, H. Yin, P. Liu, Y. Long, W. Li and J. Fan, Controllable $Cs_xFA_{1-x}PbI_3$ Single-Crystal Morphology via Rationally Regulating the Diffusion and Collision of Micelles toward High-Performance Photon Detectors, *ACS Appl. Mater. Interfaces*, 2019, **11**, 13812–13821.

39 D. Ju, X. Jiang, H. Xiao, X. Chen, X. Hu and X. Tao, Narrow Band Gap and High Mobility of Lead-Free Perovskite Single Crystal Sn-Doped $MA_3Sb_2I_9$, *J. Mater. Chem. A*, 2018, **6**, 20753–20759.

40 P. Szklarz, A. Gągor, R. Jakubas, P. Zieliński, A. Piecha-Bisiorek, J. Cichos, M. Karbowiak, G. Bator and A. Cizman, Lead-Free Hybrid Ferroelectric Material Based on Formamidine: $[NH_2CHNH_2]_3Bi_2I_9$, *J. Mater. Chem. C*, 2019, **7**, 3003–3014.

41 P. Szklarz, A. Pietraszko, R. Jakubas, G. Bator, P. Zieliński and M. Gałazka, Structure, Phase Transitions and Molecular Dynamics of $[C(NH_2)_3]_3[M_2I_9]$, M = Sb, Bi, *J. Phys.: Condens. Matter*, 2008, **20**, 255221.

42 P. Szklarz, A. Gągor, R. Jakubas, W. Medycki and G. Bator, Temperature Symmetry Breaking and Properties of Lead-Free Organic–Inorganic Hybrids: Bismuth(III) Iodide and Antimony(III) Iodide: $(S(CH_3)_3)_3[Bi_2I_9]$ and $(S(CH_3)_3)_3[Sb_2I_9]$, *Dalton Trans.*, 2023, **52**, 11981–11991.

43 M. Węcławik, A. Gągor, R. Jakubas, A. Piecha-Bisiorek, W. Medycki, J. Baran, P. Zieliński and M. Gałązka, Structure–Property Relationships in Hybrid $(C_3H_5N_2)_3[Sb_2I_9]$ and (C3H5N2)3[Bi2I9] Isomorphs, *Inorg. Chem. Front.*, 2016, **3**, 1306–1316.

44 K. M. McCall, C. C. Stoumpos, O. Y. Kontsevoi, G. C. B. Alexander, B. W. Wessels and M. G. Kanatzidis, From 0D $Cs_3B_2I_9$ to 2D $Cs_3Bi_2I_6Cl_3$: Dimensional Expansion Induces a Direct Band Gap but Enhances Electron–Phonon Coupling, *Chem. Mater.*, 2019, **31**, 2644–2650.

45 K. M. McCall, C. C. Stoumpos, S. S. Kostina, M. G. Kanatzidis and B. W. Wessels, Strong Electron–

Phonon Coupling and Self-Trapped Excitons in the Defect Halide Perovskites $A_3M_2I_9$ (A = Cs, Rb; M = Bi, Sb), *Chem. Mater.*, 2017, **29**, 4129–4145.

46 S. Valastro, S. Gavranovic, I. Deretzis, M. Vala, E. Smecca, A. La Magna, A. Alberti, K. Castkova and G. Mannino, Temperature-Dependent Excitonic Band Gap in Lead-Free Bismuth Halide Low-Dimensional Perovskite Single Crystals, *Adv. Opt. Mater.*, 2024, **12**, 1–10.

47 V. V. Nawale, T. Sheikh and A. Nag, Dual Excitonic Emission in Hybrid 2D Layered Tin Iodide Perovskites, *J. Phys. Chem. C*, 2020, **124**, 21129–21136.

48 P. I. Djurovich, E. I. Mayo, S. R. Forrest and M. E. Thompson, Measurement of the Lowest Unoccupied Molecular Orbital Energies of Molecular Organic Semiconductors, *Org. Electron.*, 2009, **10**, 515–520.

49 M. E. Kamminga, G. A. De Wijs, R. W. A. Havenith, G. R. Blake and T. T. M. Palstra, The Role of Connectivity on Electronic Properties of Lead Iodide Perovskite-Derived Compounds, *Inorg. Chem.*, 2017, **56**, 8408–8414.

50 F. Ünlü, A. Kulkarni, K. Lê, C. Bohr, A. Bliesener, S. D. Öz, A. K. Jena, Y. Ando, T. Miyasaka, T. Kirchartz and S. Mathur, Single- or double A-site cations in A3Bi2I9 bismuth perovskites: What is the suitable choice?, *J. Mater. Res.*, 2021, **36**, 1794–1804.

51 S. Meloni, G. Palermo, N. Ashari-Astani, M. Grätzel and U. Rothlisberger, Valence and Conduction Band Tuning in Halide Perovskites for Solar Cell Applications, *J. Mater. Chem. A*, 2016, **4**, 15997–16002.

52 F. Xu, T. Zhang, G. Li and Y. Zhao, Mixed Cation Hybrid Lead Halide Perovskites with Enhanced Performance and Stability, *J. Mater. Chem. A*, 2017, **5**, 11450–11461.

53 A. Y. Lee, D. Y. Park and M. S. Jeong, Correlational Study of Halogen Tuning Effect in Hybrid Perovskite Single Crystals with Raman Scattering, X-Ray Diffraction, and Absorption Spectroscopy, *J. Alloys Compd.*, 2018, **738**, 239–245.

54 P. Sarkar, A. Srivastava, S. K. Tripathy, K. L. Baishnab, T. R. Lenka, P. S. Menon, F. Lin and A. G. Aberle, Impact of Sn Doping on Methylammonium Lead Chloride Perovskite: An Experimental Study, *J. Appl. Phys.*, 2020, **127**, 125110.

55 R. Mayengbam, S. K. Tripathy and G. Palai, First-Principle Insights of Electronic and Optical Properties of Cubic Organic-Inorganic $MAGe_xPb_{(1-x)}I_3$ Perovskites for Photovoltaic Applications, *J. Phys. Chem. C*, 2018, **122**, 28245–28255.

56 Y. Ogomi, A. Morita, S. Tsukamoto, T. Saitho, N. Fujikawa, Q. Shen, T. Toyoda, K. Yoshino, S. S. Pandey, T. Ma and S. Hayase, $CH_3NH_3Sn_xPb_{(1-x)}I_3$ Perovskite Solar Cells Covering up to 1060 Nm, *J. Phys. Chem. Lett.*, 2014, **5**, 1004–1011.

57 E. Mosconi, P. Umari and F. De Angelis, *J. Mater. Chem. A*, 2015, **3**, 9208–9215.

58 H. Hasegawa, K. Kobayashi, Y. Takahashi, J. Harada and T. Inabe, Effective Band Gap Tuning by Foreign Metal Doping in Hybrid Tin Iodide Perovskites, *J. Mater. Chem. C*, 2017, **5**, 4048–4052.

59 A. L. Abdelhady, M. I. Saidaminov, B. Murali, V. Adinolfi, O. Voznyy, K. Katsiev, E. Alarousu, R. Comin, I. Dursun, L. Sinatra, E. H. Sargent, O. F. Mohammed and O. M. Bakr, Heterovalent Dopant Incorporation for Bandgap and Type Engineering of Perovskite Crystals, *J. Phys. Chem. Lett.*, 2016, **7**, 295–301.

60 Y. Yamada, M. Hoyano, R. Akashi, K. Oto and Y. Kanemitsu, Impact of Chemical Doping on Optical Responses in Bismuth-Doped $CH_3NH_3PbBr_3$ Single Crystals: Carrier Lifetime and Photon Recycling, *J. Phys. Chem. Lett.*, 2017, **8**, 5798–5803.

61 Y. Zhou, D. D. Zhou, B. M. Liu, L. N. Li, Z. J. Yong, H. Xing, Y. Z. Fang, J. S. Hou and H. T. Sun, Ultrabroad Near-Infrared Photoluminescence from Bismuth Doped CsPbI3: Polaronic Defects vs. Bismuth Active Centers, *J. Mater. Chem. C*, 2016, **4**, 2295–2301.

62 A. M. Ganose, C. N. Savory and D. O. Scanlon, Beyond Methylammonium Lead Iodide: Prospects for the Emergent Field of Ns2 Containing Solar Absorbers, *Chem. Commun.*, 2017, **53**, 20–44.

63 R. E. Brandt, V. Stevanović, D. S. Ginley and T. Buonassisi, Identifying Defect-Tolerant Semiconductors with High Minority-Carrier Lifetimes: Beyond Hybrid Lead Halide Perovskites, *MRS Commun.*, 2015, **5**, 265–275.

64 Z. Zhang, L. Ren, H. Yan, S. Guo, S. Wang, M. Wang and K. Jin, Bandgap Narrowing in Bi-Doped $CH_3NH_3PbCl_3$ Perovskite Single Crystals and Thin Films, *J. Phys. Chem. C*, 2017, **121**, 17436–17441.

65 F. N. Mansoorie, P. Bhatt, A. Tewari, R. Kumar and M. Bag, Unveiling the Impact of Bi^{3+} Heterovalent Doping on the Negative Capacitance and Ionic Conductivity of Perovskite Single Crystals: Implication in Neuromorphic Computing, *ACS Appl. Mater. Interfaces*, 2025, **17**, 4218–4230.

66 M. Yu, S. Yang, C. Wu and N. Marom, Machine Learning the Hubbard U Parameter in DFT+U Using Bayesian Optimization, *npj Comput. Mater.*, 2020, **6**, 180.

67 I. Spanopoulos, W. Ke, C. C. Stoumpos, E. C. Schueller, O. Y. Kontsevoi, R. Seshadri and M. G. Kanatzidis, Unraveling the Chemical Nature of the 3D "Hollow" Hybrid Halide Perovskites, *J. Am. Chem. Soc.*, 2018, **140**, 5728–5742.

68 C. R. Pidgeon, in *Encyclopedia of Modern Optics*, ed. R. D. Guenther, Elsevier, Oxford, 2005, pp. 426–432.

69 O. I. Kucheriv, H. R. Petrosova, V. Y. Sirenko, O. A. Semenikhin, M. Choghaei, K. Meerholz, S. Olthof and I. A. Gural'skiy, Aziridinium 3D Perovskites: Toward Semiconducting Films with Tunable Band Gaps, *Chem. Mater.*, 2025, **37**, 4758–4767.

70 B. H. Toby and R. B. Von Dreele, GSAS-II : the genesis of a modern open-source all purpose crystallography software package, *J. Appl. Crystallogr.*, 2013, **46**, 544–549.

71 P. H. T. Philipsen, G. te Velde, E. J. Baerends, J. A. Berger, P. L. de Boeij, M. Franchini, J. A. Groeneveld, E. S. Kadantsev, R. Klooster, F. Kootstra, M. C. W. M. Pols, P. Romaniello, M. Raupach, D. G. Skachkov, J. G. Snijders, C. J. O. Verzijl, J. A. Celis Gil, *et al.*, BAND 2024.1, SCM, Theoretical Chemistry, Vrije Universiteit, Amsterdam, The Netherlands, **https://www.scm.com**.

72 G. te Velde and E. J. Baerends, Precise Density-Functional Method for Periodic Structures, *Phys. Rev. B:Condens. Matter Mater. Phys.*, 1991, **44**, 7888–7903.
73 P. H. T. Philipsen, E. van Lenthe, J. G. Snijders and E. J. Baerends, Relativistic Calculations on the Adsorption of CO on the (111) Surfaces of Ni, Pd, and Pt within the Zeroth-Order Regular Approximation, *Phys. Rev. B:Condens. Matter Mater. Phys.*, 1997, **56**, 13556–13562.
74 P. H. T. Philipsen and E. J. Baerends, Relativistic Calculations to Assess the Ability of the Generalized Gradient Approximation to Reproduce Trends in Cohesive Properties of Solids, *Phys. Rev. B:Condens. Matter Mater. Phys.*, 2000, **61**, 1773–1778.